PROCEEDINGS OF SPIE

SPIEDigitalLibrary.org/conference-proceedings-of-spie

Airways, vasculature, and interstitial tissue: anatomically informed computational modeling of human lungs for virtual clinical trials

Ehsan Abadi, Gregory Sturgeon, Greeshma Agasthya, Brian Harrawood, Christoph Hoeschen, et al.

Ehsan Abadi, Gregory M. Sturgeon, Greeshma Agasthya, Brian Harrawood, Christoph Hoeschen, Anuj Kapadia, W. Paul Segars, Ehsan Samei, "Airways, vasculature, and interstitial tissue: anatomically informed computational modeling of human lungs for virtual clinical trials," Proc. SPIE 10132, Medical Imaging 2017: Physics of Medical Imaging, 101321Q (9 March 2017); doi: 10.1117/12.2254739



Event: SPIE Medical Imaging, 2017, Orlando, Florida, United States

Airways, vasculature, and interstitial tissue: anatomically-informed computational modeling of human lungs for virtual clinical trials

Ehsan Abadi*^a, Gregory M. Sturgeon^a, Greeshma Agasthya^a, Brian Harrawood^a, Christoph Hoeschen^b, Anuj Kapadia^a, W. Paul Segars^a, Ehsan Samei^a

^aCarl E. Ravin Advanced Imaging Laboratories, NC, United States;

^bHelmholtz Zentrum Muenchen, Germany

ABSTRACT

This study aimed to model virtual human lung phantoms including both non-parenchymal and parenchymal structures. Initial branches of the non-parenchymal structures (airways, arteries, and veins) were segmented from anatomical data in each lobe separately. A volume-filling branching algorithm was utilized to grow the higher generations of the airways and vessels to the level of terminal branches. The diameters of the airways and vessels were estimated using established relationships between flow rates and diameters. The parenchyma was modeled based on secondary pulmonary lobule units. Polyhedral shapes with variable sizes were modeled, and the borders were assigned to interlobular septa. A heterogeneous background was added inside these units using a non-parametric texture synthesis algorithm which was informed by a high-resolution CT lung specimen dataset. A voxelized based CT simulator was developed to create synthetic helical CT images of the phantom with different pitch values. Results showed the progressive degradation in depiction of lung details with increased pitch. Overall, the enhanced lung models combined with the XCAT phantoms prove to provide a powerful toolset to perform virtual clinical trials in the context of thoracic imaging. Such trials, not practical using clinical datasets or simplistic phantoms, can quantitatively evaluate and optimize advanced imaging techniques towards patient-based care.

Keywords: Computational phantom, CT simulator, Lung modeling, XCAT phantoms.

1. INTRODUCTION

The extended cardiac-torso (XCAT) library of computational phantoms have been extensively developed for medical imaging research and optimization^{1,4}. These phantoms have surface-based representations of roughly 9000 anatomical structures which were segmented from patient imaging datasets and further enhanced by Visible Male and Female anatomical datasets from National Library of Medicine^{5, 6}. A drawback to these phantoms, however, is that the small vasculature and heterogeneous parenchymal background of the lungs are not modeled. These detailed structures are essential for the XCAT models to be applicable to image quality based evaluations in thoracic imaging, one of the most frequent image acquisitions in medical imaging.

In terms of lung anatomy, the human lung has five lobes: three on the right and two on the left. Each lobe can be classified into two main regions: non-parenchyma and parenchyma. The non-parenchymal region is defined as the pulmonary vessel and airway trees with diameters greater than 0.2 mm ⁷. Generally, the non-parenchyma structures are volume-filling networks with tubular shapes bifurcating 16 generations to the level of terminal branches^{8, 9}. The parenchyma is defined as the remaining background anatomy including air, lymphatics, pulmonary acinus (gas exchange units), connective tissue septa, capillaries, etc. Secondary pulmonary lobules are the smallest units of the lung parenchyma which are separated and marginated by connective tissue septa¹⁰. These units have irregular polyhedral shapes with variable sizes¹⁰.

The purpose of this study was to advance the XCAT phantoms by modeling the lung non-parenchyma and parenchyma structures for a more realistic lung architecture and then demonstrate the use of these models in the context of thoracic imaging. In this study, both non-parenchyma and parenchyma structures were modeled and incorporated into XCAT phantoms. Then, a voxelized-based ray tracer was developed to create synthetic CT projections of the phantoms. Finally, as a pilot study, the impact of different pitch values was evaluated in terms of the depiction of lung details in the synthesized CT images.

Medical Imaging 2017: Physics of Medical Imaging, edited by Thomas G. Flohr, Joseph Y. Lo, Taly Gilat Schmidt, Proc. of SPIE Vol. 10132, 101321Q · © 2017 SPIE CCC code: 1605-7422/17/\$18 · doi: 10.1117/12.2254739

2. MATERIALS AND METHODS

2.1 Modeling the lung non-parenchyma

The current XCAT phantoms include manually segmented initial branches of the pulmonary airways and vessels up to 9 generations. Since these segmentations were limited by the image acquisition, not all the non-parenchyma structures could be extracted. Therefore, an anatomically-based volume-filling algorithm¹¹ was applied to estimate and add cylindrical models of the higher generation branches of the airways, arteries, and veins to the level of terminal bronchioles, arterioles, and venules. Figure 1 shows a diagram of the growth model. This algorithm was designed to iteratively estimate the bifurcation points of the new generations of the airways, arteries, veins, and their corresponding diameters, and centerlines. At each iteration, the phantom was updated by adding the newly generated structures, avoiding potential intersections. The intersections were identified using a binary mask of the previous structures. Then the centerlines of the intersected branches were moved along the gradient descent of the signed Euclidean transform map of the mask until the intersections were cleared. The algorithm was repeated to grow a given branch until at least one of the following conditions was met: 1) branch length was less than 1.2 mm ¹¹, 2) diameter was less than 0.2 mm ⁷, or 3) 16 bifurcations were obtained. Finally, the algorithm ended when no branch was eligible to bifurcate. The diameters of the synthesized branches were estimated based on the investigated relationships between the flow and diameters of pulmonary airways and vessels¹².

Growth model

- 1: Segment the lobes and initial branches of airways, arteries, and veins
- 2: Calculate ending points and centerlines of the branches
- 3: Choose airway, artery, and vein in a loop
- 4: Find the ending points which are eligible to bifurcate
- 5: Partition the free space inside the lobes with Voroni diagram using ending points
- 6: Calculate the center of mass in each sub-division
- 7: In each sub-division, find a plane that includes the center of mass, starting and ending points of the parent branch
- 8: Using the defined plane, bisect each sub-division into two regions
- 9: Calculate the center of mass in the new regions
- 10: Locate the bifurcation points 40% along the vector including the parent ending points and the center of mass points
- 11: Estimate the diameters and centerlines
- 12: Revise the centerlines in case of intersections
- 13: Update the phantom with the new generated structure
- 14: If the ending points are not terminal, go to 3
- 15: End

Figure 1. Outline of the growth model for the lung airways, arteries, and veins

2.2 Modeling the lung parenchyma

The geometry of the secondary pulmonary lobule units was modeled as irregular polyhedral shapes with variable sizes based on anatomy literature 10 . This was done by finding random points inside the lung parenchyma regions and calculating the Voronoi diagram of the seed points. Number of seed points was estimated as V_p/V_{splu} , where V_p is the total volume of the parenchymal regions and V_{splu} is the average volume of a secondary pulmonary lobule unit, which from literature was 300 mm³. The boundaries of the Voronoi diagram were assigned to be the connective tissue septa with an average thickness of 0.1 mm 10 . Then, using a high -resolution (0.114 mm) CT dataset of a lung specimen 13 as the volumetric exemplar, a unique texture instance was synthesized for each of the secondary pulmonary lobules. This was done by first segmenting 30 volumes of interests (VOIs) within the secondary pulmonary lobules of the high-resolution CT dataset. Then, informed by these VOIs, random parenchymal textures were synthesized using a non-parametric texture synthesis algorithm 14 and incorporated inside the defined secondary pulmonary lobule units. Each synthesized volume was randomly initialized with a similar histogram as one of the VOIs. Voxel by voxel, in a 3D raster scan order, the synthesized volumes were updated based on the 3D causal neighborhood similarity with the exemplar VOIs. L_2 norm was used as a similarity metric between the neighborhoods of the synthesized and the exemplar volumes. A window size of 11 was used for the causal neighborhood since this size is on the order of structures within the secondary pulmonary lobules.

2.3 Voxelizing the final phantom

Both the non-parenchyma and parenchyma structures were synthesized at an isotropic resolution of 0.1 mm then down-sampled to 0.25 mm to place inside a voxelized XCAT phantom. The target 0.25 mm resolution is roughly twice as fine as the resolution of commercially available scanners.

2.4 Imaging with a voxelized-based helical CT simulator

A helical ray tracer was developed based on a commercial CT scanner (SOMATOM Definition, Siemens Healthcare, Forchheim, Germany) geometry and spectrum. Using the Geant4 toolkit¹⁵, at each projection angle, the path lengths of the source rays intersecting the voxels of the phantom were measured. Then, signal S at the detector element i,j at the projection angle α was calculated as

$$S(i,j,\alpha) = -\ln(\frac{\sum_{E} E \ poisson(N_{E,i,j,\alpha}e^{-\sum_{m} \mu_{m,E,i,j,\alpha}l_{m,i,j,\alpha}})}{\sum_{E} N_{E,i,j,\alpha}E}), \tag{1}$$

where $N_{E,i,j,\alpha}$ is the number of photons arriving at the detector element i,j at the angle α and at the energy bin of E (accounting for bowtie filter spectrum) without attenuation, $\mu_{m,E,i,j,\alpha}$ is the linear attenuation coefficient of the material m at the energy bin of E, and $l_{m,i,j,\alpha}$ is the intersection length between photons reaching detector i,j and voxels with material m. The projection images were reconstructed using a weighted filtered backprojection algorithm for helical fan-beam CT scans¹⁶.

2.5 A pilot virtual clinical trial

XCAT phantoms with the detailed lung structures can be used to quantify image quality metrics in thoracic imaging which are not feasible using simplistic/uniform phantoms or real human datasets. As a pilot study, we quantified the impact of pitch values in helical scans in terms of containing lung structure details. Synthetic CT scans of an XCAT phantom were obtained with pitch of 0.5, 1, 2, and 4. The CT images with pitch of 0.5 was assumed to contain the most structural details in the lungs comparing with the other acquired datasets. A comparison was made between pitch of 0.5 and other pitch values to quantify how much details are lost in the higher pitch values. To do so, resulting images with pitch of 1, 2, and 4 were subtracted from pitch of 0.5 and then normalized by pitch of 0.5.

3. RESULTS

The lung phantom non-parenchyma before and after the growth model are shown in Figure 2. The added non-parenchyma structures were found to produce results in the range of human anatomy in terms of diameters, branch lengths, angles, and number of generations^{8, 9, 17}.

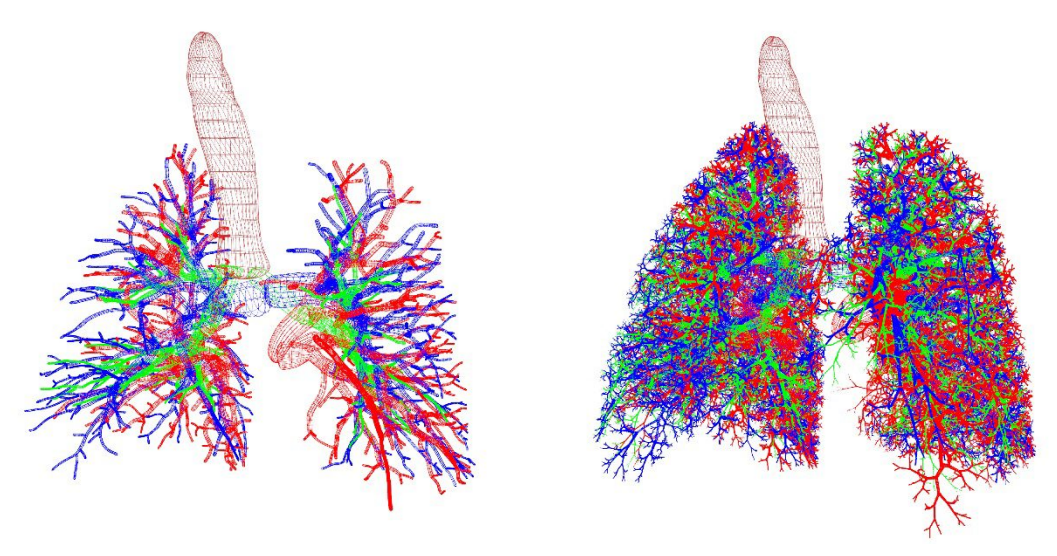


Figure 2. (Left) Initial segmented airways and vessels. (Right) Result of the growth model. Airways are green, arteries are blue, and veins are red.

Some slices of the voxelized phantom including the newly generated non-parenchyma and added parenchyma structures are shown in Figure 3. Reconstructed CT images with and without the inclusion of non-parenchyma and parenchyma are shown in Figure 4. Results show the improvement of the realism in the CT images with modeling the non-parenchyma and parenchyma structures inside the lung.

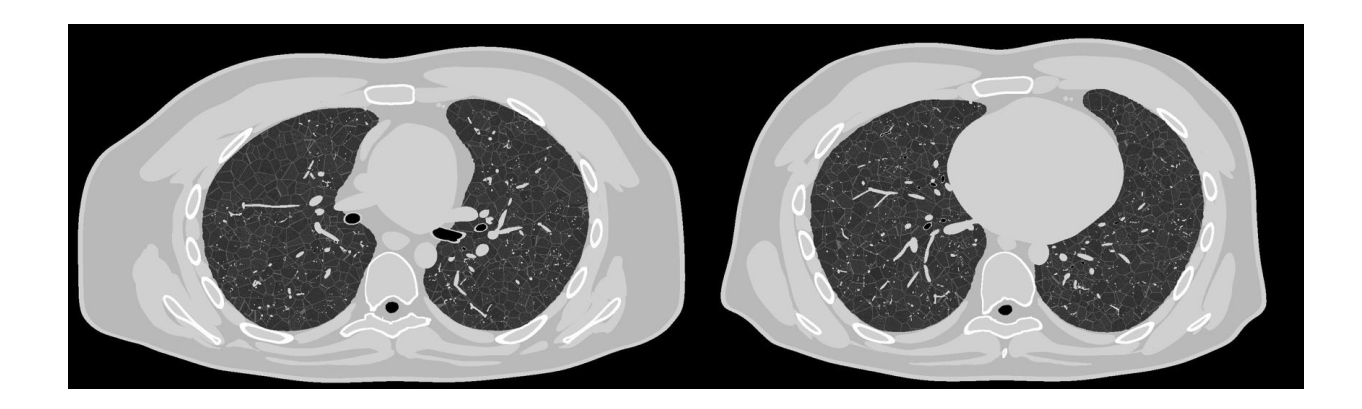


Figure 3. Example slices (left and right) of the voxelized phantom including parenchyma and non-parenchyma structures inside the lungs of an XCAT phantom. The resolution of the phantom is 0.25×0.25×0.25 mm³. Different intensities in the phantom indicate different materials.

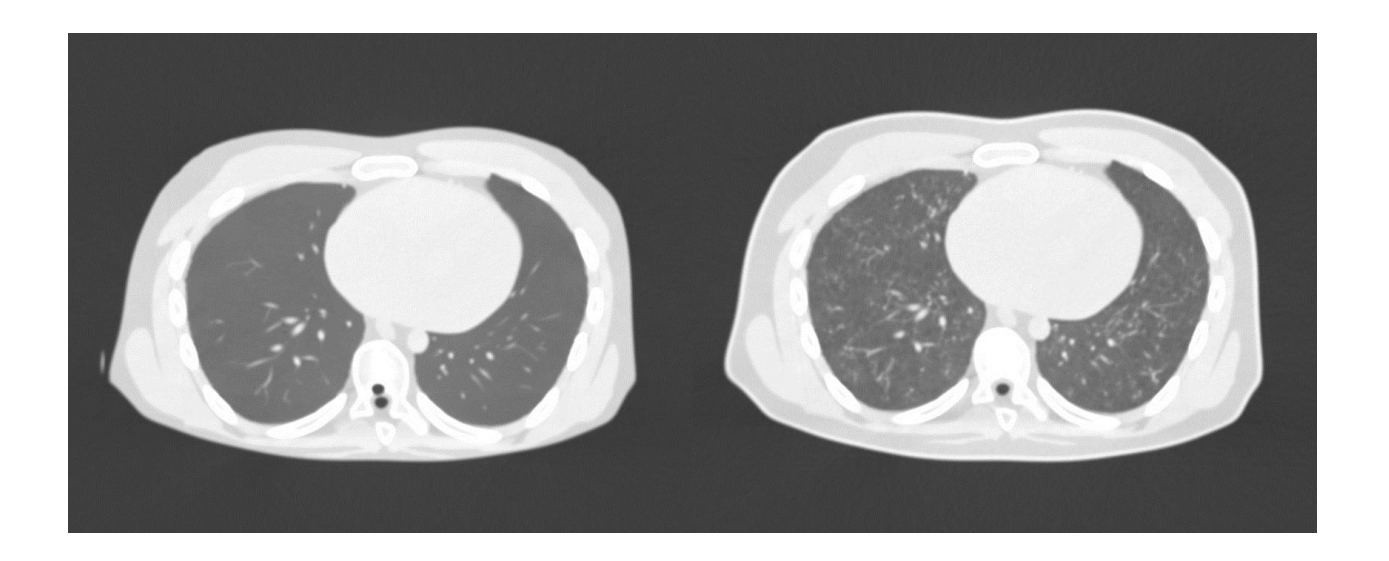


Figure 4. CT images simulated from the XCAT phantom without (left) and with (right) the lung non-parenchyma and parenchyma modeling. Window=1600, Level=-600.

Finally, the reconstructed CT images with pitch of 0.5, 1, 2, and 4 are shown in Figure 5. CT images with pitch of 0.5 and 1 were found to be free of strong artifacts; however, small helical artifacts were found in pitch of 2. The relative percentage difference between pitch of 0.5 and pitches of 1, 2, and 4 were 3%, 8%, and 97%, respectively, indicating the progressive degradation of 3D rendition with increased pitch. Pitch of 4 represented a gross under-sampling of the phantom geometry.

4. CONCLUSION

Modeling non-parenchyma and parenchyma structures increase the realism of the XCAT phantoms. This will facilitate their use in clinically relevant simulation studies of image quality. These studies can be utilized to optimize current and emerging medical imaging technologies to achieve a desired diagnostic image quality while minimizing dose, time, and/or cost of imaging. Future work will focus on validation of the phantoms with observer studies and conducting simulation experiments which would not be feasible using simplistic phantoms or real human datasets

5. ACKNOWLEDGMENT

This study was supported by a research grant from National Institutes of Health (2R01EB001838). The authors gratefully acknowledge Dr. Helmut Schlattl for providing the lung specimen dataset, and Dr. Justin Solomon and Wanyi Fu for their valuable comments and feedback.

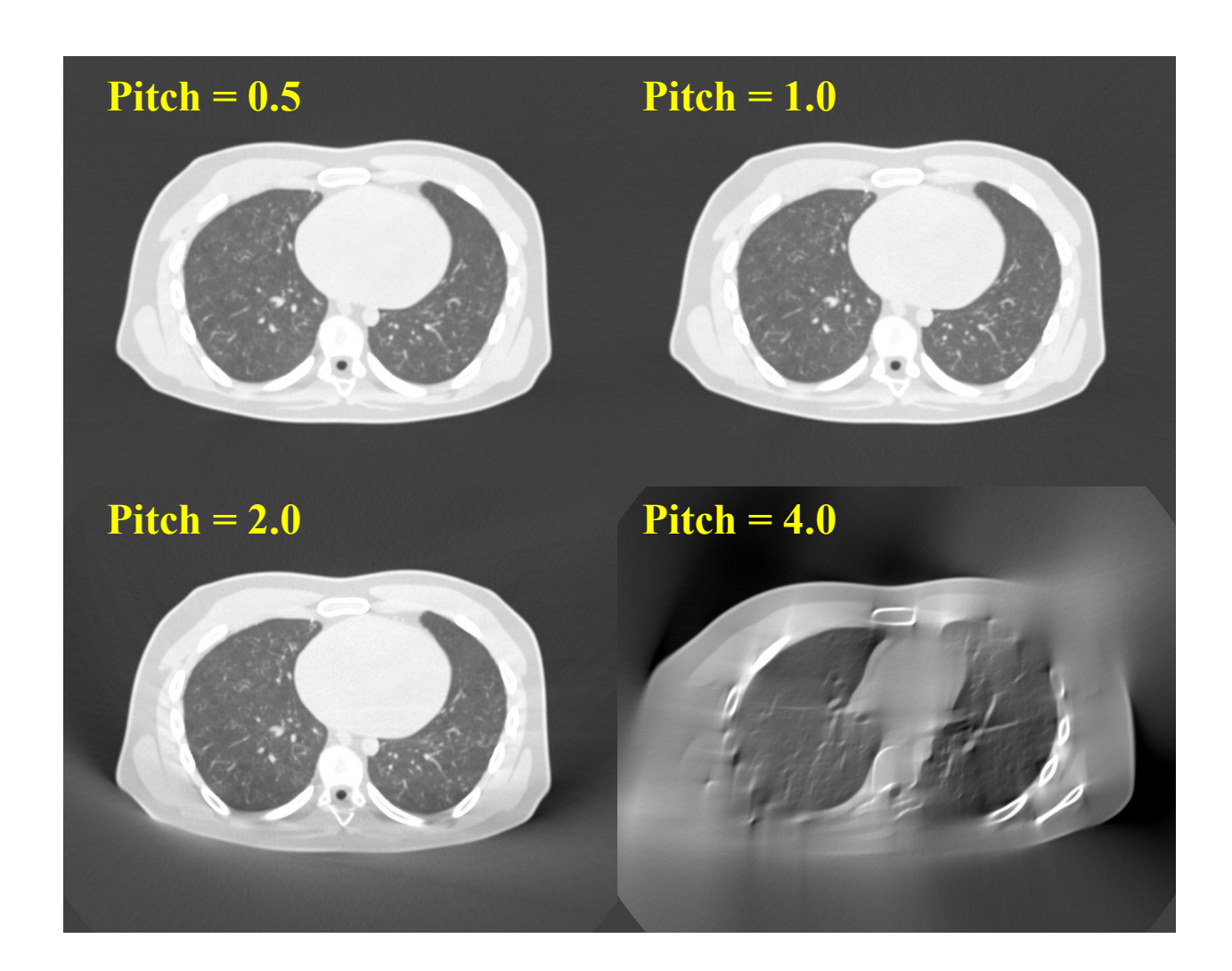


Figure 5. Helical CT images simulated from the XCAT phantom with different pitches. Window=1600, Level=-600.

REFERENCES

- [1] W. Segars, M. Mahesh, T. Beck, E. Frey, B. Tsui, "Realistic CT simulation using the 4D XCAT phantom," Medical physics **35**, 3800-3808 (2008).
- [2] W.P. Segars, J. Bond, J. Frush, S. Hon, C. Eckersley, C.H. Williams, J. Feng, D.J. Tward, J. Ratnanather, M. Miller, "Population of anatomically variable 4D XCAT adult phantoms for imaging research and optimization," Medical physics **40**, 043701 (2013).
- [3] W. Segars, G. Sturgeon, S. Mendonca, J. Grimes, B.M. Tsui, "4D XCAT phantom for multimodality imaging research," Medical physics **37**, 4902-4915 (2010).
- [4] W. Segars, H. Norris, G.M. Sturgeon, Y. Zhang, J. Bond, A. Minhas, D.J. Tward, J. Ratnanather, M. Miller, D. Frush, "The development of a population of 4D pediatric XCAT phantoms for imaging research and optimization," Medical physics **42**, 4719-4726 (2015).

- [5] M. Ackerman, V. Spitzer, A. Scherzinger, D. Whitlock, "The Visible Human data set: an image resource for anatomical visualization," Medinfo. MEDINFO 8, 1195-1198 (1994).
- [6] V. Spitzer, M.J. Ackerman, A.L. Scherzinger, D. Whitlock, "The visible human male: a technical report," Journal of the American Medical Informatics Association 3, 118-130 (1996).
- [7] M.I. Townsley, "Structure and composition of pulmonary arteries, capillaries, and veins," Comprehensive Physiology, (2012).
- [8] K. Horsfield, G. Cumming, "Morphology of the bronchial tree in man," Journal of Applied Physiology 24, 373-383 (1968).
- [9] W. Huang, R. Yen, M. McLaurine, G. Bledsoe, "Morphometry of the human pulmonary vasculature," Journal of Applied Physiology **81**, 2123-2133 (1996).
- [10] W.R. Webb, "Thin-Section CT of the Secondary Pulmonary Lobule: Anatomy and the Image—The 2004 Fleischner Lecture 1," Radiology **239**, 322-338 (2006).
- [11] M.H. Tawhai, P. Hunter, J. Tschirren, J. Reinhardt, G. McLennan, E.A. Hoffman, "CT-based geometry analysis and finite element models of the human and ovine bronchial tree," Journal of applied physiology **97**, 2310-2321 (2004).
- [12] H. Kitaoka, R. Takaki, B. Suki, "A three-dimensional model of the human airway tree," Journal of Applied Physiology **87**, 2207-2217 (1999).
- [13] N. Petoussi-Henss, J. Becker, M. Greiter, H. Schlattl, M. Zankl, C. Hoeschen, "Construction of anthropomorphic hybrid, dual-lattice voxel models for optimizing image quality and dose in radiography," SPIE Medical Imaging, International Society for Optics and Photonics (2014).
- [14] L.-Y. Wei, M. Levoy, "Fast Texture Synthesis using Tree-structured Vector Quantization," In Proceedings of the 27th annual conference on Computer graphics and interactive techniques, ACM Press/Addison-Wesley Publishing Co, 479-488 (2000).
- [15] S. Agostinelli, J. Allison, K.a. Amako, J. Apostolakis, H. Araujo, P. Arce, M. Asai, D. Axen, S. Banerjee, G. Barrand, "GEANT4—a simulation toolkit," Nuclear instruments and methods in physics research section A: Accelerators, Spectrometers, Detectors and Associated Equipment **506**, 250-303 (2003).
- [16] J. Hoffman, S. Young, F. Noo, M. McNitt-Gray, "Technical Note: FreeCT_wFBP: A robust, efficient, open-source implementation of weighted filtered backprojection for helical, fan-beam CT," Medical physics 43, 1411-1420 (2016).
- [17] K.S. Burrowes, P.J. Hunter, M.H. Tawhai, "Anatomically based finite element models of the human pulmonary arterial and venous trees including supernumerary vessels," Journal of applied physiology **99**, 731-738 (2005).